

ARTICLE OPEN



The evolution of pit morphology and growth kinetics in aluminum during atmospheric corrosion

Philip J. Noell¹✉, Erin Karasz¹, Eric J. Schindelholz², Andrew T. Polonsky¹, Ian Campbell³, Ryan M. Katona¹ and Michael A. Melia¹

Assessing the lifetimes of alloys in humid, corrosive environments requires growth kinetic information regarding individual instances of damage, e.g. pit growth rates. Corrosion rates measured at the continuum scale using mass change convolute the rate of pit nucleation and growth, providing limited information on local kinetics. The current study used in-situ X-ray computed tomography to measure growth rates of individual pits in aluminum over 100 h of exposure in a humid, chloride environment. While pits grew at relatively constant rates over the first hours after nucleation, significant growth-rate nonlinearities subsequently occurred. These were linked to both droplet spreading, which altered the cathode size, and changes in the mode of pit growth. Pit morphology appeared to influence the dominant growth mode and the duration of pit growth. Post-mortem serial sectioning revealed pits preferentially attacked grain-boundary triple junctions and dislocation boundaries.

npj Materials Degradation (2023)7:12; <https://doi.org/10.1038/s41529-023-00328-7>

INTRODUCTION

Predicting the lifetimes of metallic components in humid, chloride environments remains a central challenge in the field of materials science¹. A key impediment to assessing the growth kinetics of localized corrosion damage such as pits is the necessity of characterizing sub-surface damage evolution without interrupting the evolving electrochemical processes. Atmospheric corrosion rates drawn from mass change provide little information about how the size and shape of pits or other localized damage evolve with time². Component failure is often driven by the evolution of these individual damage events rather than the rate of corrosion across the entire component^{2–6}. To directly characterize corrosion over extended periods without significantly altering the evolving process, 3D imaging methods such as X-ray computed tomography (XCT) provide an appealing alternative to mass change measurements^{2,7}. In the present study, 3D imaging tools were used to measure rates of pit growth and characterize how pit morphology evolves during atmospheric corrosion of aluminum.

Using both laboratory and synchrotron-based XCT, multiple researchers have demonstrated the effectiveness of capturing the complex materials degradation phenomena related to corrosion^{3,6–17}. With a spatial resolution on the order of one micron and a temporal resolution on the order of minutes to hours, XCT is ideal for capturing long-term kinetic data of the entire life cycle (nucleation, growth, and death) of individual pitting events, uniquely so under atmospheric environments⁸. It must be noted that the submicron features XCT misses can be important for determining corrosion initiation and propagation mechanisms, such as the tunneling phenomena observed in Al or metastable pitting activities¹⁸. Post-mortem sectioning using focused ion beam (FIB) and scanning electron microscopy (SEM) can thus augment in-situ XCT data, e.g. to assess relationships between corrosion damage and the microstructure at submicron length scales^{19,20}.

In-situ XCT has been used to study both the kinetics of corrosion damage and how it evolves relative to the microstructure in steel and aluminum alloys immersed in chloride solutions^{3,6–17}. Electrochemical polarization has been employed to

provide direct relationships between electrochemical measurements and corrosion damage morphology^{4,7,21}. Because corrosion under immersed and atmospheric conditions are often incomparable²², in-situ XCT has also been used to measure pit growth rates and the evolution of environmentally assisted cracking in humid, atmospheric, and chloride-containing environments^{19,22–26}.

Two studies in particular focused on the growth kinetics of pits during atmospheric corrosion. Glanvill et al.²⁶ measured the growth kinetics of a single pit over 35 min in Al 2024 at a 5-min temporal resolution. The volume of this pit increased at a roughly linear rate. Its morphology evolved irregularly, with only a small part of the pit active at any given time. The relationship between the morphology of this pit and the microstructure was not assessed, though the authors suggested that intergranular corrosion may have occurred. In commercial-purity aluminum, using a 7 h temporal resolution, it was determined that pits generally grew at constant rates up to repassivation except when droplet spreading occurred¹⁹. After droplet spreading, the rate of pit growth increased substantially, suggesting a strong tie between the electrolyte at the surface and the local kinetic response of the pit. In both cases, no clear explanation of why pits grew at relatively constant rates was given.

Building on prior studies, this work seeks to understand the interplay between droplet electrolyte conditions, pitting damage kinetics, pit morphology, and the underlying microstructure by using a combination of in-situ XCT and FIB-based serial sectioning to evaluate the evolving morphology and growth kinetics of pits in 99.99% (4N) purity aluminum wires. Pitting corrosion was characterized over 100 h of exposure using a temporal resolution of 80 min (1.3 h). Subsequent post-mortem serial sectioning, with ex-situ FIB, was used to assess the influence of the grain structure on the manner of pit growth.

RESULTS

Material and experimental overview

In the following we report: (1) salient details about the microstructure of the Al wire used, (2) continuum-level

¹Sandia National Laboratories, P.O. Box 5800, Albuquerque, NM 87185-0889, USA. ²The Ohio State University, Fontana Laboratories, 140W 19th Ave, Columbus, OH 43210, USA. ³Materials Science and Engineering Department, University of Washington, Seattle, WA, USA. ✉email: pnoell@sandia.gov

observations of corrosion, (3) the growth kinetics of individual pits, (4) the evolution of pit morphology, (5) the microscale morphology of a pit evaluated via post-mortem cross-sectioning, and (6) droplet evolution during pit growth. Four of the eleven pits observed in this study were associated with droplet spreading, which significantly affected their growth kinetics. For simplicity, we omit discussion of these pits until the final paragraphs of this section.

Secondary electron images and electron backscatter diffraction (EBSD) data showing the microstructure of the 4N-Al wire used in this study are provided in Supplementary Figs. 1 and 2. Grains were elongated along the drawing direction. The average grain length was 262 μm and the average grain diameter was 61 μm . EBSD revealed the presence of dislocation boundaries typical of cold-worked Al²⁷.

Exposure of four replicate Al wires loaded with 200 $\mu\text{g}/\text{cm}^2$ of NaCl microparticles to 84% relative humidity (RH) resulted in a total of 11 observable pits that nucleated and grew over the first 100 h after exposure. The total area inspected by the XCT measurements for an individual Al wire was 3.2 mm^2 ; thus a total of 12.8 mm^2 was inspected over all four wires. The number of pits on a given sample varied from 1 to 6. Pit nucleation is defined as the first timestep at which the pit volume equaled or exceeded 15.6 μm^3 , the minimum resolvable feature size within these XCT data. All pits ceased measurable growth within the 100-h period examined.

Cumulative volume loss

A typical distribution of pits (blue circles) on one of the Al wire samples is shown in Fig. 1a. This 3D rendering shows droplets (dark gray) and the Al wire (light gray). Notably, each pit nucleated and grew under a separate, non-neighboring droplet relative to other pits on that sample. For a given sample, multiple pits were observed to nucleate and grow simultaneously. All pits observed in this study nucleated at the edge of droplets, see top-down views in Figures (b) and (c).

The number of pits observed across these four samples is provided on the plot in Fig. 2a as a function of time after exposure. Combining measured pit volumes from all four samples, cumulative volume loss is provided as a function of exposure time in Fig. 2b. Both datasets were normalized by the measured surface area. We note that pits were observed under a limited number of droplets on each wire. This may be related to many reasons, including the underlying surface characteristics or the initiation time.

Cumulative volume loss exhibits stepwise sigmoidal growth kinetics. Sigmoidal growth kinetics are defined as having (1) an initial stage of exponential growth followed by (2) a stage of growth at a roughly constant rate until (3) the growth rate slows until the pit volume reaches an asymptote. After reaching an initial asymptote ≈ 50 h after exposure, Figure(b) shows that volume increased again before approaching a second asymptote ≈ 85 h after exposure. This coincided with the nucleation, growth, and repassivation of a single pit, see Fig. 2a.

To evaluate the rate of volume loss during each regime of sigmoidal growth, the slope of the linear stage of each regime was measured. This follows methods described elsewhere for evaluating the growth rate of sigmoidal functions^{28,29}, though we note that many descriptors exist for sigmoidal growth kinetics. These rates were 1059 and 634 $\mu\text{m}^3/\text{h}$ (83 and 50 ($\mu\text{m}^3/\text{h})/\text{mm}^2$ when normalized by surface area) for these two regimes of growth.

Growth kinetics of individual pits

Plots of pit volume as a function of time for four pits representative of the seven pits not associated with droplet spreading are provided in Figs. 3 and 4. After reaching an initial asymptote, the volume of all pits increased by $\approx 20\%$. Measurable

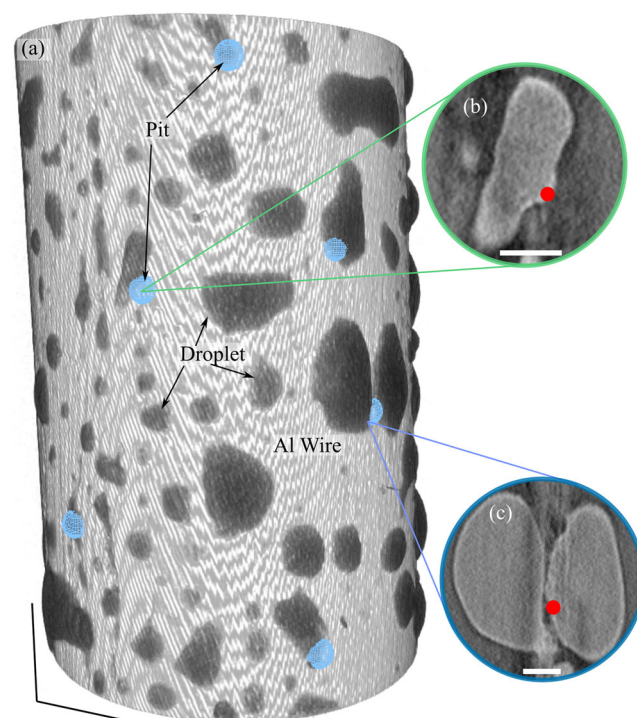


Fig. 1 Three-dimensional rendering of wire. A 3D rendering of a wire sample upon which 6 pits nucleated is provided in a, scale bars are 200 μm . The spatial location of each of these pits is indicated with a blue hemisphere and droplets are the darker gray contrast on the Al wire surface. Top-down views of the droplets associated with two pits are provided in b and c, scale bars are 50 μm . Red circles mark the location beneath which these pits nucleated. Markers are included to indicate location and do not indicate pit size.

pit growth subsequently ceased for the remainder of the period characterized during this study. As highlighted in Figs. 3 and 4, we define the growth before and after this asymptote as the initial and secondary growth regimes.

During the initial growth regime, the growth kinetics of individual pits were nonlinear. They can be described as roughly sigmoidal. The divisions provided in Fig. 3 highlight these three stages of growth. Due to the 80-min temporal resolution used in this study, only 2 data points were captured in the exponential and asymptotic growth regimes for several pits and the labels shown in Fig. 3 are suggestions rather than definitive statements of when transitions from one stage to another occurred.

Pit growth rates during the initial growth regime, i.e. initial growth rates, were measured using the slope of the linear stage of this growth regime, see Fig. 4, and are reported in Table 1. Notably, initial growth rates varied by as much as 10% depending on the region designated as the linear growth region. These uncertainties are included in Table 1.

For all pits excepting the two pits shown in Fig. 4, the secondary growth regime lasted less than 5 h; it lasted 19 h or more for the two pits shown in Fig. 4. This relatively short secondary growth duration limits assessment to determine what function(s), e.g. sigmoidal, best fit the secondary growth regime. For simplicity, pit growth rates during the secondary growth regime were assessed using a linear function (see Figs. 3 and 4) and are provided in Table 1. In all cases, secondary growth rates were slower than initial growth rate.

Initial and secondary pit growth rates as a function of initial droplet size are provided in Fig. 5a. The initial droplet size is defined as the volume of the droplet in the first timestep after pit nucleation. The duration of pit growth as a function of either initial

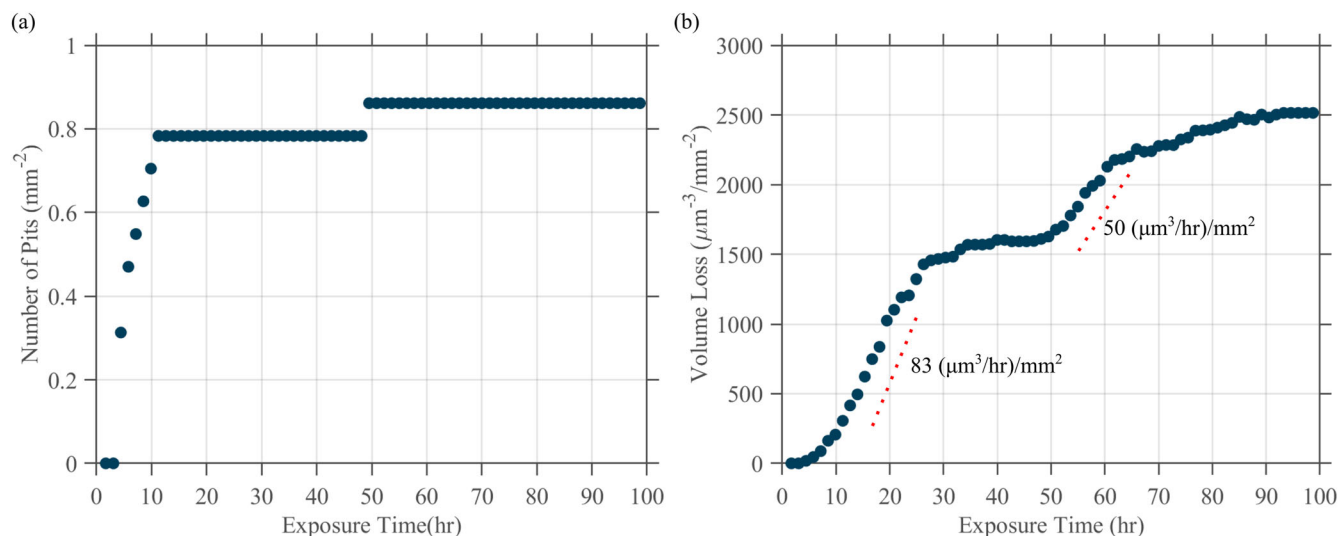


Fig. 2 Continuum-level characteristics of pitting. Combining data from all four samples, plots of the cumulative number of pits per unit area and the cumulative volume loss per unit area as a function of time are shown in **a** and **b**, respectively. These data are normalized by the surface area characterized using XCT.

pit growth rate or initial droplet size are provided in Fig. 5b, c. The duration of pit growth is defined as the period elapsed between the timestep preceding the first timestep at which the pit was observed until the last timestep at which any measurable growth occurred. Note that these figures include data from the four pits associated with droplet spreading.

For the seven pits not associated with droplet spreading, within the resolution of XCT data, the transition from the initial to the secondary growth regime was neither associated with droplet spreading nor other significant changes to the droplet, e.g. droplet merging. To highlight this, 3D renderings and 2D tomographs showing the evolving morphologies of pits 1 and 2 and their accompanying droplets are presented in Figs. 3c–g and 4c–g, respectively.

The transition from the initial to the secondary growth regime was associated with a change in the manner in which pit morphology evolved, as is now described. The evolving morphology of pits 1 and 2 during the initial growth regime are shown in Figs. 3c–f and 4c–f, respectively. During this regime, pits primarily grew by the formation and extension of tendrils away from a central pit body. This arborescent-like mode of pit growth will be referred to as mode 1 growth. Note that many volumes within the pits shown in these figures appear to be physically separated from one another. These volumes were likely connected by tunnels that were below the $15.6 \mu\text{m}^3$ minimum resolvable feature size.

The evolving morphology of these pits during the secondary growth regime are shown in Fig. 3g–h and Fig. 4g–h. During this period, corrosion occurred on nearly the entire surface of the pit. Rather than creating new tendrils, existing tendrils expanded radially. This mode of pit growth will be referred to as mode 2 growth. The most dramatic example of the mode 2 growth can be seen in Fig. 4, where the overall morphology of the pit changed relatively little over the final 24 h of its life, but the volume increased by more than $4000 \mu\text{m}^3$ as existing tendrils expanded radially.

During the initial growth regime, mode 1 and mode 2 growth appeared to occur simultaneously, though most volume appeared to be added via mode 1 growth. During the secondary growth regime, no mode 1 growth was observed. Instead, all observable pit growth was mode 2 growth.

From the pit volume data for pits 1 and 2 and their accompanying change in surface area, estimates for the average current density of each pit over a single time interval were

calculated. These are shown in Fig. 6a. For both pits, the current density dropped to zero when no measurable change in volume and/or surface area occurred. From the current density values, pit stability product ($i \cdot x$) values could be tabulated with respect to time for both pits. These are shown in Fig. 6b, c. Since pitting occurred at multiple depths throughout a pit's life, a spread of ($i \cdot x$) values were calculating using 1D diffusion distances from 2 to $50 \mu\text{m}$ for pit 1 and 2 to $120 \mu\text{m}$ for pit 2, respectively. The maximum diffusion distance chosen was based on the furthest distance a pit tendrils propagated from the original pit mouth and the minimum was based on the resolution limit of the XCT. For reference, the red lines and shaded area are the range of ($i \cdot x$) values associated with metastable and stable pitting for Al, respectively^{30,31}. The current density reported in Fig. 6 should be regarded as the local current density. Because the real local current density evolves significantly faster than the 80 min temporal resolution of this study, the estimation reported in Fig. 6 may include errors. These data are thus a best estimate based upon the available data.

3D serial sectioning

To assess the microstructural features associated with tendrils, FIB serial-sectioning combined with EBSD was performed. After attempts to cross-section pits 1 and 2 failed, a pit which formed near pits 1 and 2 was selected for detailed analysis. This pit, which will be labeled pit 12, nucleated after the first 100 h of exposure; thus, the growth kinetics of pit 12 cannot be evaluated. A 3D rendering and 2D slice of pit 12 are shown in Fig. 7a, b. These reveal that its morphology consisted of both elongated tendrils similar to pit 2 and a large network of meandering tendrils similar to pit 1.

EBSD data from serial sectioning pit 12 are presented in Fig. 7c, d at different locations and orientations within the pit. These are presented as kernel average misorientation (KAM) maps with the pit volume colored blue. For these maps, all misorientations greater than or equal to 10° , i.e. high-angle grain boundaries, are assigned the same color, yellow. The KAM maps reveal how the pit propagated relative to grain and dislocation boundaries, labeled in Fig. 7c, and highlight a tendrils that propagated along a grain boundary triple line. Flythrough videos sliced parallel to the X, Y, and Z axes showing these 3D KAM maps are provided in the Supplementary Data. Note that the pit is colored red in the flythrough videos.

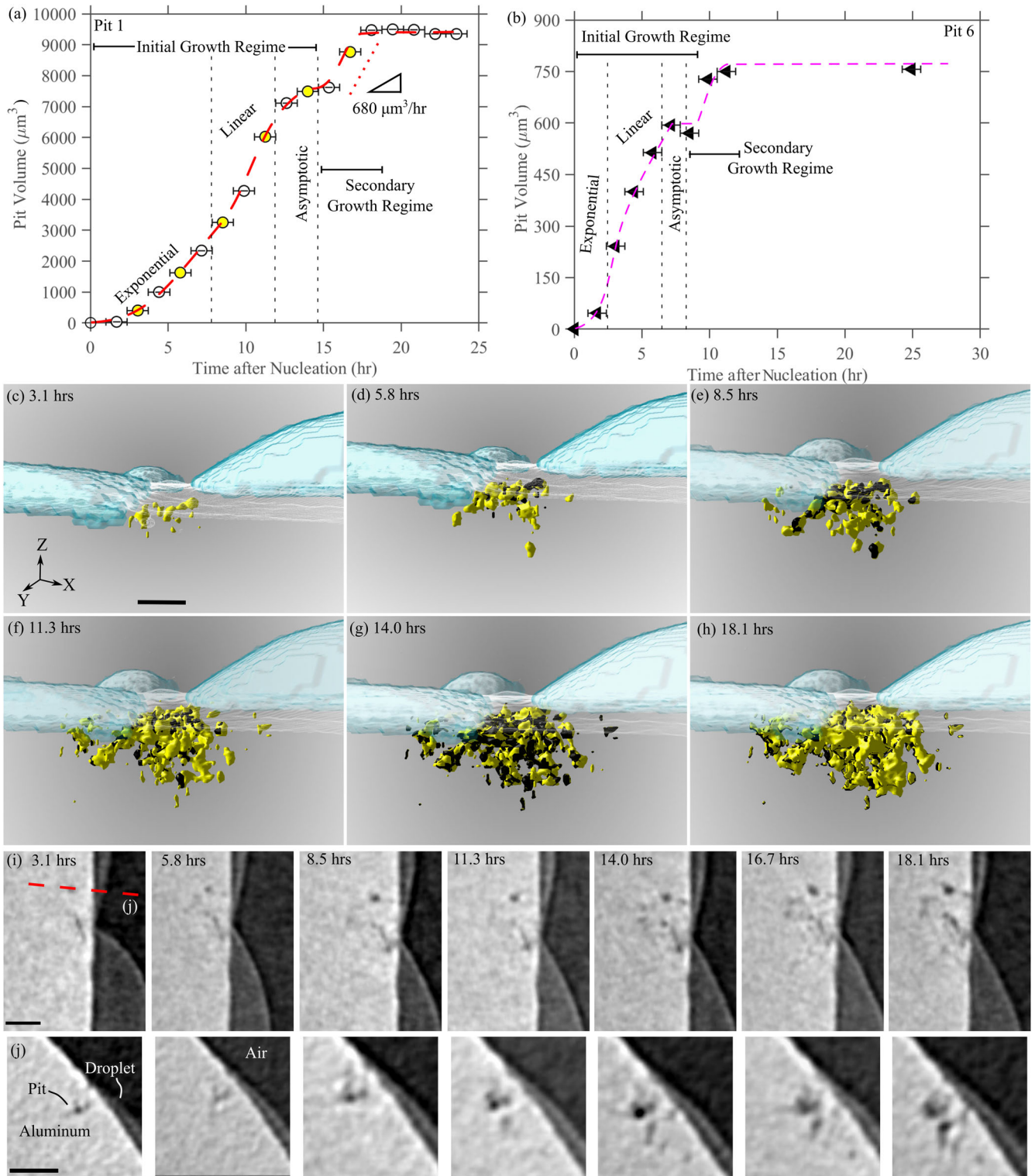


Fig. 3 Growth trends for two individual pits. Plots of pit volume as a function of time for pits 1 and 6 are provided in **a** and **b**, respectively. These exemplify pits with secondary growth regimes shorter than 5 h. 3D renderings of pit 1 at the timesteps highlighted yellow in **a** are provided in **c** to **h**, all at the same scale. Yellow represents new growth from the previous time step and black represents previous growth. 2D slices of pit 1 at multiple time steps are provided in **i** and **j**. In the 2D slices, black regions are air, dark gray regions are the droplet, the light gray is the Al metal, and the dark gray within the metal is the pit. Error bars represent measurement uncertainty in time as described in the “Methods” section. Scale bars in **c**, **i**, and **j** are 25, 20, and 20 μm , respectively.

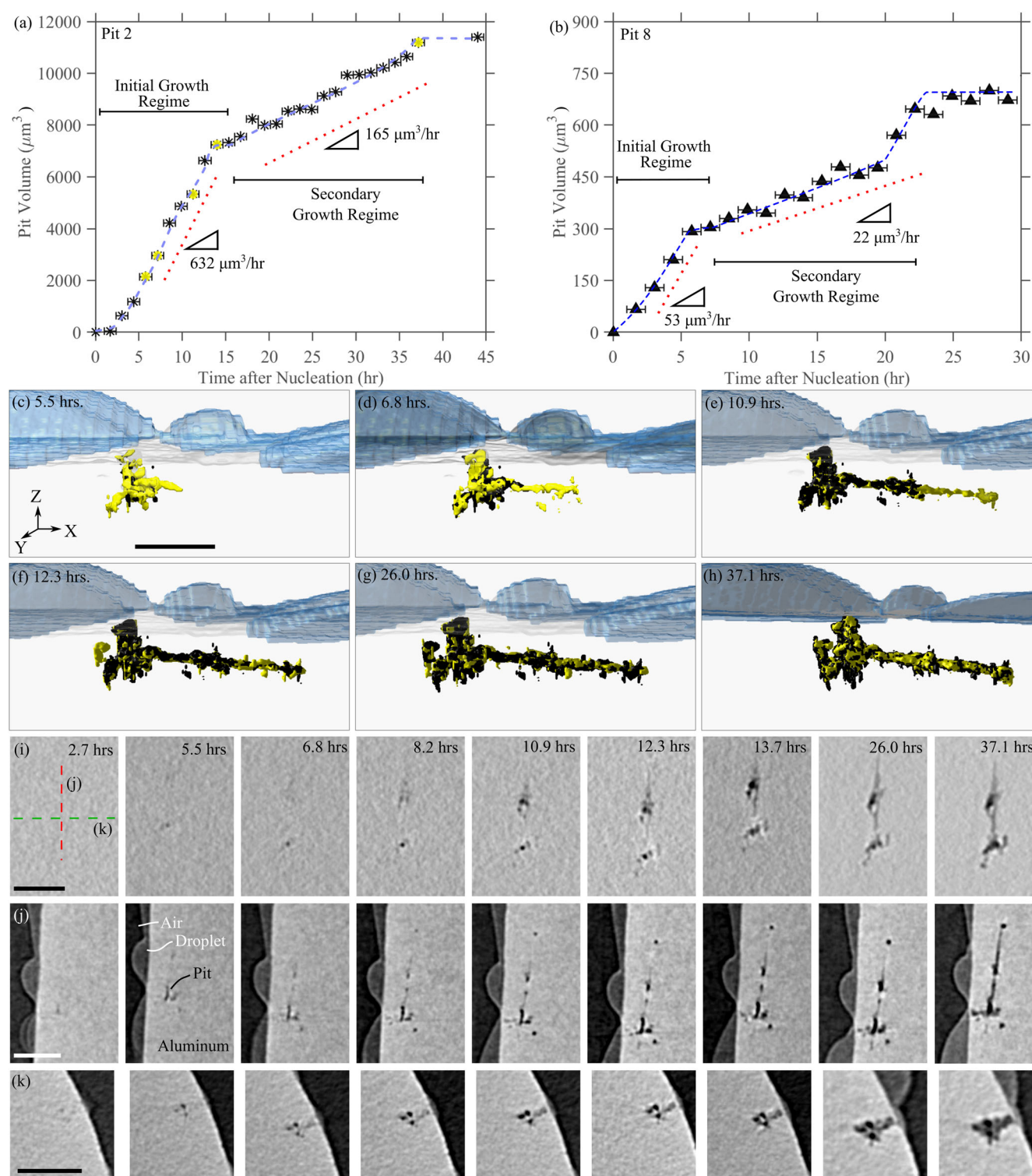


Fig. 4 Growth trends for two individual pits with extended periods of mode 2 growth. Plots of pit volume as a function of time for pits 2 and 8 are provided in **a** and **b**, respectively. These pits exemplify pits with secondary growth regimes greater than 5 h. 3D renderings of pit 2 at the timesteps highlighted yellow in **a** are provided in **c** to **h**, all at the same scale. Yellow represents new growth from the previous time step and black represents previous growth. 2D slices of pit 2 at multiple time steps are provided in **i** to **k**. In the 2D slices, black regions are air, dark gray regions are the droplet, the light gray is the Al metal, and the dark gray within the metal is the pit. Error bars represent measurement uncertainty in time as described in the “Methods” section. Scale bars in **c**, **i**, **j**, and **k** are 50 μm .

An inverse pole figure (IPF) map of the grain structure around the pit at the same slice as that shown in Fig. 7c is provided in (e). IPF coloring is relative to the surface normal the Z-axis defined in Fig. 7a. These images highlight that the pit grew selectively in

grains oriented with a $\{111\}$ normal to the wire surface. A secondary electron image from the same 2D slice as Fig. 7c, e is presented in Fig. 7f. The surface of the pit was smooth as opposed to a sharp, crystallographic etching-type morphology.

Table 1. The initial pit growth rate secondary growth rate (if applicable) post-spreading growth rate (if applicable) the growth duration and the final volume are shown for all eleven pits Growth rate calculations assumed a linear trend Pits 3 4 and 5 were associated with multiple post-spreading growth rates The average and standard deviation of these growth rates are provided Plus minus for in initial growth rate measurements reflect uncertainty in defining the linear stage.

	Pit 1	Pit 2	Pit 3	Pit 4	Pit 5	Pit 6	Pit 7	Pit 8	Pit 9	Pit 10	Pit 11
Initial growth rate ($\mu\text{m}^3/\text{h}$)	825 ± 75	634 ± 11	68 ± 8	145 ± 16	76 ± 6	124 ± 9	71 ± 6	53 ± 5	108 ± 10	121 ± 10	103 ± 6
Secondary growth rate ($\mu\text{m}^3/\text{h}$)	680	165	–	–	–	114	–	22	73	54	59
Post-spreading growth rates ($\mu\text{m}^3/\text{h}$)	–	–	235 ± 60	253 ± 16	115 ± 11	–	60	–	–	–	–
Growth duration (h)	18.1	37.3	19.4	31.8	30.4	9.9	19.4	24.9	12.6	7.2	12.6
Final pit volume (μm^3)	9497	11402	1856	3601	2166	757	839	743	547	394	502

Droplet spreading

The plots of pit volume as a function of time provided Fig. 8a, b are characteristic of the four pits associated with droplet spreading. For all of these pits, all measurable growth ceased 5 to 10 hours after the pit nucleated. After a period of inactivity, which ranged from 1.3 to 6.5 h, one or more secondary droplets formed near the pit mouth at the edge of the main droplet. This is highlighted in Fig. 8c–e. In all cases, in the timestep immediately after this secondary droplet formed, measurable pit growth resumed and continued for several hours. The secondary droplet also continued to grow and spread. For some pits, including both shown in Fig. 8, this cycle of growth stagnation followed by a significant increase in pit volume occurred multiple times. These cycles were not clearly tied to the formation of new secondary droplets or significant changes in the volume of the droplet.

Prior to droplet spreading, the growth kinetics of these four pits could generally be described as sigmoidal. Pre-spreading pit growth rates were measured from the linear growth stage for these four pits and are provided in Table 1. The temporal resolution of this study was insufficient to determine the function best describing the post-spreading growth kinetics. As shown in Fig. 8, a range of post-spreading growth rates could be approximated as the linear slope of each stepped region. The average and standard deviation of these post-spreading growth rates are provided in Table 1.

DISCUSSION

In-situ XCT combined with 3D serial sectioning reveals the complex evolution of pit morphology and growth kinetics in relationship to the local electrolyte and microstructure. These measurements provide baseline data for comparisons to pit growth models and provide insights into the dominant corrosion mechanisms. To clarify the factors common to the growth of all pits observed in this study, we begin by presenting an overview of the lifecycle of an individual pit, see Fig. 9. Subsequently, we discuss four key questions in light of the results of this study: (1) what governs the rate of pit growth, (2) what governs the lifespan of an individual pit, (3) how can droplet spreading affect the rate of pit growth, and (4) how does the cumulative corrosion rate compare to the growth rate of individual pits?

Pits nucleated at the edge of droplets, likely at specific microstructural features susceptible to pitting, see Fig. 9b. Notably, Al generally has excellent corrosion resistance due to the dense oxide film on its surface and this must be compromised by chloride ions before pit nucleation can occur^{32,33}. Nucleation at a droplet edge, where a relatively higher flux of oxygen is expected than near the droplet center, suggests that oxygen flux was critical to nucleation³⁴. In Al alloys, pits have been observed to preferentially nucleate at the intersection of droplet edges with microstructural features susceptible to pitting, e.g. intermetallic particles^{35–37}. In the absence of intermetallic particles, pits are

known to preferentially attack grain boundaries, dislocation boundaries, and grains oriented with the {111} plane normal to the surface^{19,38}. Regarding the latter, it is known that, in Al, the pitting potential of the {111} plane is relatively low compared to other orientations^{19,38}. Metastable pitting events below the resolution of XCT likely occurred underneath many droplets but never achieved the conditions for stable pitting, perhaps due to a lack of cathodic current to meet the anodic current demand of the pit^{39,40}.

Drawing from extensive literature on aluminum corrosion^{41,42}, we briefly describe the likely electrochemical processes within the pit. As shown in Fig. 9b, the cathode exists in the droplet surrounding the pit's mouth and possibly extends to adjacent droplets if thin water layers, including monolayers, exist connecting them. Chloride ions (Cl^-) diffuse from the cathode to the anode, i.e. the base of the pit highlighted orange in Fig. 9b. Metal hydrolysis occurs at the anode, reducing pH. The cathode consumes O_2 and generates OH^- , increasing pH. Corrosion product forms in the cathode and near the pit mouth, increasing Ohmic drop.

After nucleation, pit volume increases roughly exponentially as the pit grows normal to the wire's surface, forming the pit mouth. Eventually, the rate of pit growth reaches a maximum value and remains at this rate for several hours as tendrils extend from the pit mouth along susceptible microstructural features, see Fig. 9c. A constant pit growth rate indicates that the separation and IR drop between the anode and cathode remain relatively constant. During this period, both mode 1 and mode 2 growth likely occur simultaneously, see Fig. 9d, though most volume is added by mode 1 growth. As individual tendrils extend away from the cathode, ohmic drop within them increases until further growth of that tendril can no longer be sustained and growth within the tendril slows below the resolution of the XCT, possibly to complete repassivation.

Under the constant salt loading and humidity conditions, tendrils propagate in an arborescent manner along preferred pathways, shown in the plasma FIB serial sectioning analysis from Fig. 7 to be associated with dislocation boundaries, grain boundaries, or susceptible crystal facets such as the {111} planes for Al (observed to be bound by {100} type planes)^{43–45}. Additionally, the widely spaced Fe-rich particles present in this material may lead to preferential corrosion near these particles. This highly selective attack is indicative of a limitation in corrosion kinetics to the point where only the weakest microstructural features are capable of being corroded. At the leading interface of a pit front, the phenomena known as tunneling may occur as well, which tends to propagate along specific grain orientations at a feature size around 1 μm in diameter (below the resolution of the XCT)^{18,43,46}.

Eventually two factors cause the growth rate of the entire pit to slow, see Fig. 9d, e. First, accumulation of corrosion product within the pit increases ohmic drop between the cathode and anode⁴⁷. Secondly, the migration of Al^{3+} and OH^- ions into the droplet

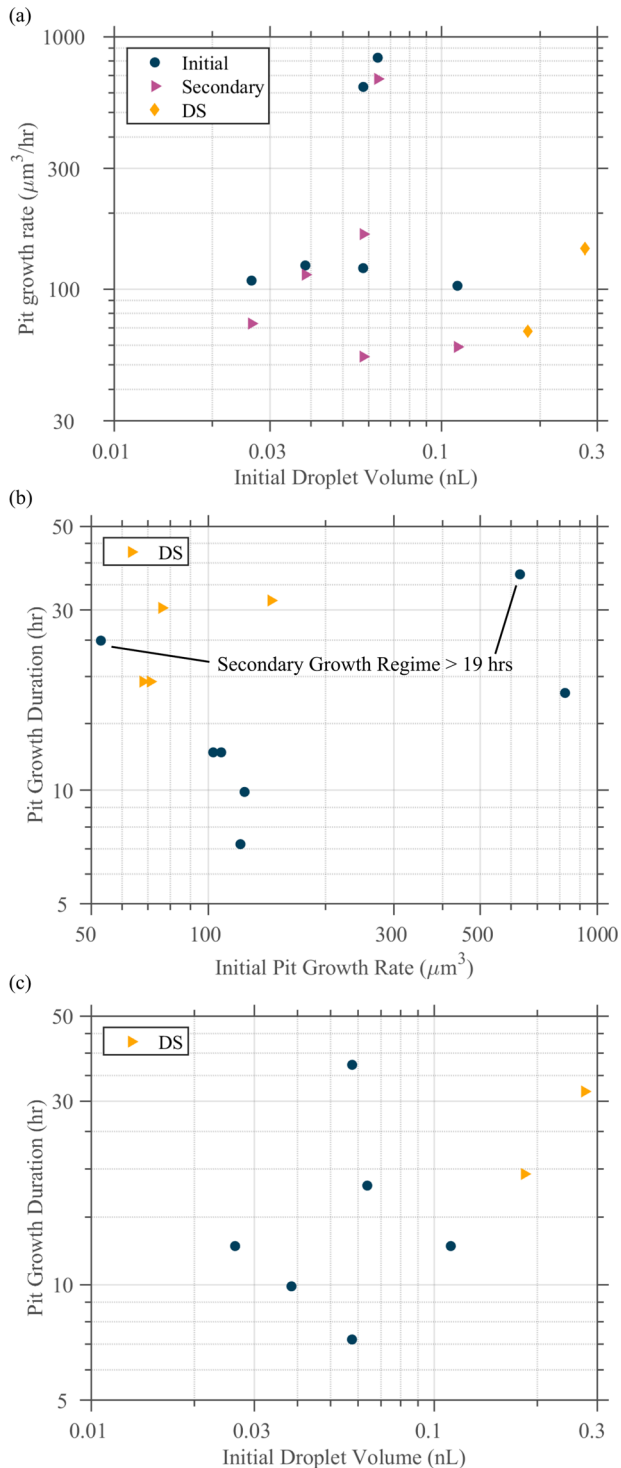


Fig. 5 Trends in growth rates and pit growth duration. Plots of **a** the initial and secondary pit growth rates as a function of initial droplet size, **b** the duration of pit growth as a function of initial pit growth rate, and **c** the duration of pit growth as a function of initial droplet size are provided. Pits associated with droplet spreading (DS) are highlighted separately. Note that the droplets associated with 3 pits extended outside the region of interest – these pits are excluded from these figures.

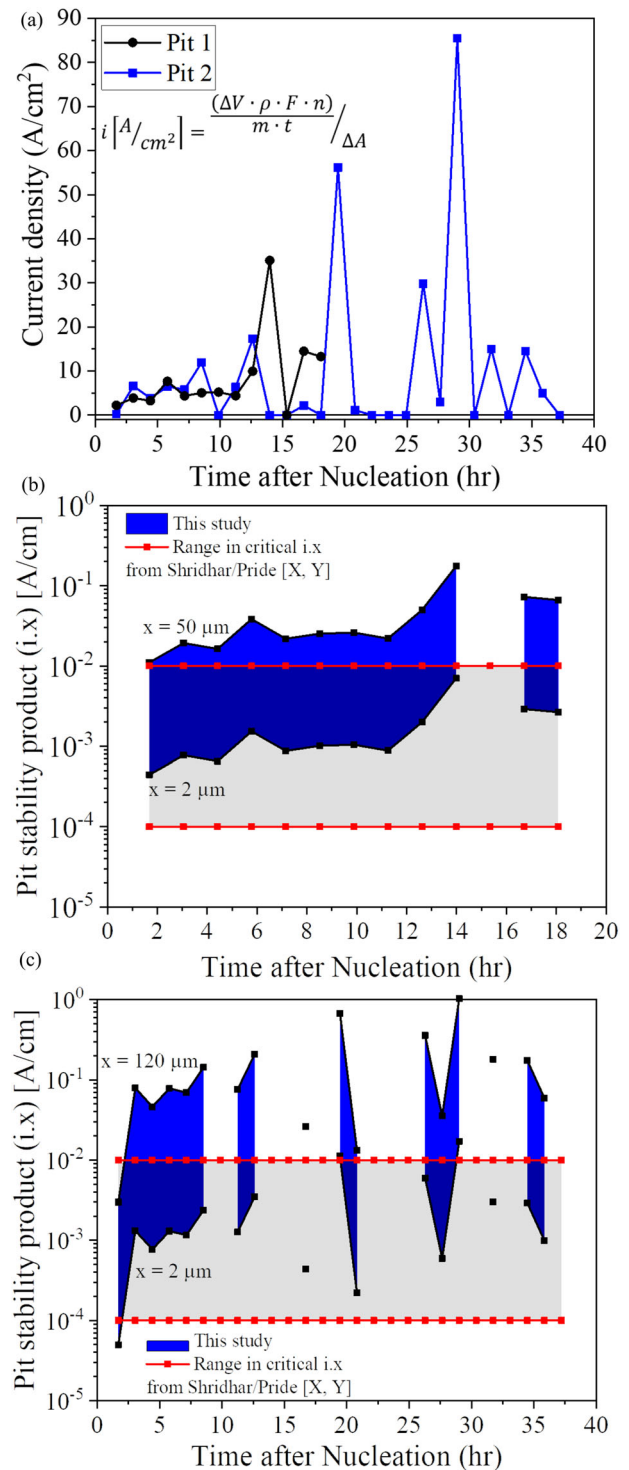


Fig. 6 Electrochemical characteristics of pitting. Estimated current density versus time for pits 1 and 2 based on XCT data in **a**; see Supplementary Material for details on the equation used to calculate this. Pit stability product (i·x) calculations for **b** pit 1 and **c** pit 2 versus time. The (i·x) was calculated for two different x values to show the range over which the product could have varied over during the life of the pit. The red lines and gray shaded region are indicative of expected pit stability product values for Al with the upper bound (10^{-2}) being for transition to stable pitting while the lower bound (10^{-4}) is a threshold value above which metastable pits have been observed to eventually stabilize.

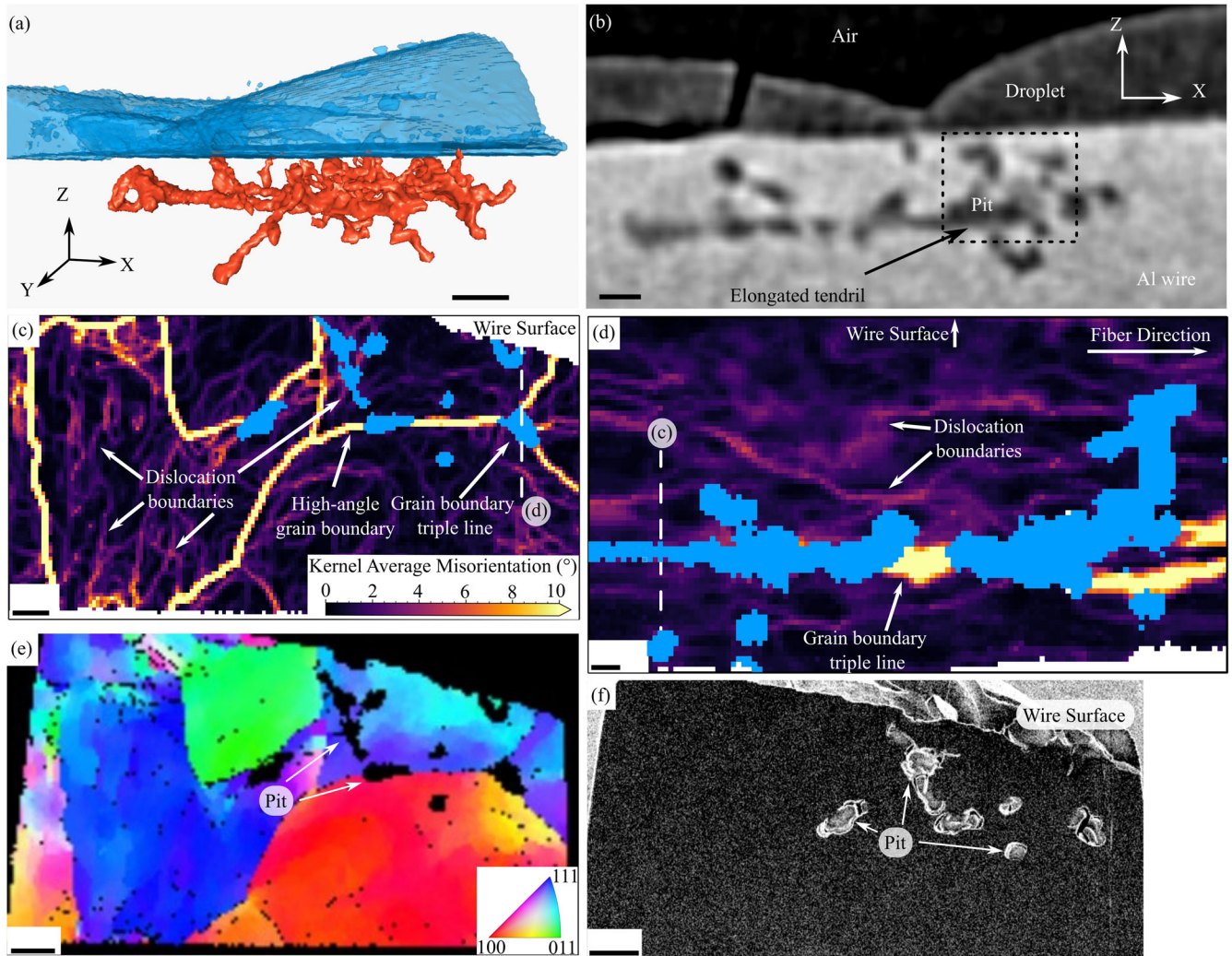


Fig. 7 Serial sectioning of an individual pit. A 3D rendering of Pit 12 is shown in **a**. A 2D tomographic slice of this pit is provided in **b**. KAM maps in **c** and **d** show a cross section of this tendril and a view of this tendril parallel to its direction of propagation. All misorientations in the KAM map greater than or equal to 10° are assigned the same color, i.e. yellow, and are associated with high-angle ($>10^\circ$) grain boundaries. Unindexed pixels that are not part of the pit are colored white. The pit is colored blue. An inverse pole figure (IPF) map showing the same slice as shown in **c** is provided in **e**. Coloring is relative to the surface normal, designated as Z in **a** and **b**. A SEM image of the pit at the slice corresponding to the EBSD data provided in **e** is shown in **f**. Scale bars in **a** to **f** are 20, 10, 5, 2.5, 10, and 10 μm , respectively.

leads to the crystallization of Al/Na carbonate rich phases, drying out the droplet and stifling cathodic kinetics⁴¹. Once the anodic overpotential drops below some critical level due to ohmic drop and stifled cathodic kinetics, see Fig. 9e, the extension of tendrils further from the pit mouth is no longer supported^{41,48}. Thereafter, the aggressive pit electrolyte chemistry formed by metal hydrolysis at the anode could help destabilize the passive film and maintain pitting conditions. However, due to ohmic drop, the pit may only be capable of supporting small, confined areas of corrosion, i.e. mode 2 growth. We note that this may explain why, during the secondary growth regime of some pits, volume increased sporadically followed by extended periods when no measurable growth occurred. Such a conclusion is supported by observing how mode 2 growth evolved in pit 2, see Fig. 4. During this growth regime, the rate and duration of mode 2 pit growth depends, in part, on the diffusion rate of these pit stabilizing species, e.g. H^+ , away from the interior of the pit. Eventually, a combination of increasing ohmic drop and droplet drying causes the available cathodic current to decrease below the level necessary to maintain mode 2 growth, and the entire pit repassivates.

Finally, changes in droplet chemistry can lead to a thin layer of concentrated electrolyte at the edge of a droplet, see Fig. 9d. This could cause droplet spreading, creating a new cathodically active region and causing the rate of corrosion to increase. For aluminum and other alloys in humid environments, droplet spreading by the formation of secondary droplets is commonly observed around NaCl and MgCl_2 drops associated with active pits^{35,49–51}. It can be caused either by the creation of OH^- ions near the edge of the electrolyte by oxygen reduction or hydrogen evolution or by metal ions produced by corrosion migrating from the pit into the droplet. These are termed cathodic and anodic spreading, respectively. In both cases, under equilibrium conditions, the added ionic species (Al^{3+} or OH^-) near the edge of a droplet can lead to the absorption of more water, causing the droplet to grow and spread^{35,50}. Calculations of the amount of water which must be absorbed during droplet spreading to maintain equilibrium in the droplet at 84% RH are provided in Supplementary Table 1.

The sequence described in the previous paragraphs produced pits having piecewise sigmoidal and linear growth kinetics. Sigmoidal growth kinetics are observed in many natural systems, e.g. population growth in the presence of limited resources⁵², and

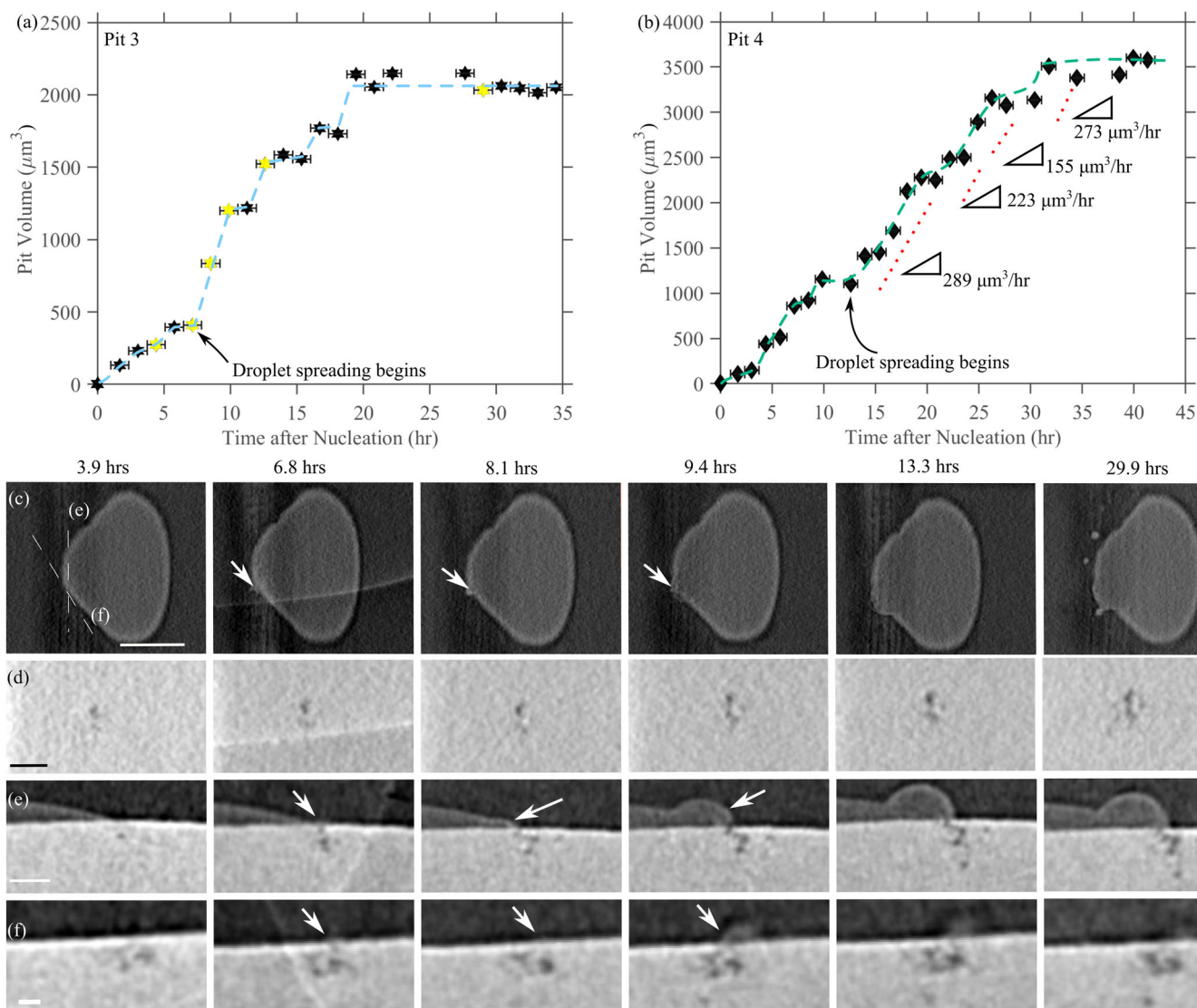


Fig. 8 Examples of pits which exhibited droplet spreading. Plots of pit volume as a function of time after pit nucleation for two pits, pits 3 and 4, associated with droplet spreading are provided in **a** and **b**. Images in **c** to **f** show 2D slices of tomography data at 1 timestep before and 5 timesteps after droplet spreading for the pit whose growth kinetic data is provided in **a**. **c**, **d** show top-down views of the droplet and pit, respectively. The locations of the cross-sections shown in **e** and **f** are highlighted in **a**. Error bars represent measurement uncertainty in time as described in the “Methods” section. Due to the limited temporal resolution of this study, the measured secondary rates are best estimates based on available data. Scale bars in **c**, **d**, **e**, and **f** are 100, 25, 25, and 25 μm , respectively.

suggest that pits gradually repassivated as the cathode dried and/or as ohmic drop exceeded a maximum. These observed kinetics are in contrast to previous reports of pit growth kinetics using either mass-loss data or in-situ XCT. The power-law growth kinetics often reported from mass-loss measurements⁵³ may primarily be a function of the rate of pit nucleation rather than indicative of individual pit growth rates¹⁹. Because, at a sufficiently low temporal resolution, sigmoidal growth kinetics appear linear, the linear growth kinetics observed in our prior study of commercial-purity Al¹⁹ was likely an artifact of the limited temporal resolution of that study compared to the present study, 7 versus 1.3 h. Lastly, while Glanvill et al. reported linear growth kinetics of a single pit in 2024 Al, only the first 35 min of this pit’s life were observed²⁶. It is possible that significant nonlinearities subsequently developed that were not captured in this study.

The previous section discussed several factors that affect the kinetics of pit growth, including droplet size, local microstructure, and pit morphology. The coupling between these factors is

complex and is challenging to discern in the experimental data presented in this study. These may be decoupled more readily in modeling studies such as references^{47,54,55}.

Because pit size is governed by both the rate and duration of pit growth, we now consider the factors that control these in light of the results of this study. The initial growth rates of pits varied by more than an order of magnitude, from 53 to 835 $\mu\text{m}^3/\text{h}$. A similar range, 30–439 $\mu\text{m}^3/\text{h}$, was observed in our previous study of commercial-purity Al exposed at 84% RH¹⁹. Noell et al. also observed that the growth rates of individual pits in commercial-purity Al increased with increasing initial droplet size¹⁹. In the current study, no relationship was observed between initial droplet volume and either the initial or secondary growth rates, see Fig. 5a. It is possible that the cathode associated with each pit may have extended beyond its droplet, which would be the case if droplets were interconnected by thin water layers too small to be captured by XCT. The more than three time increase in salt loading in this study compared to that of Noell et al. likely resulted in a

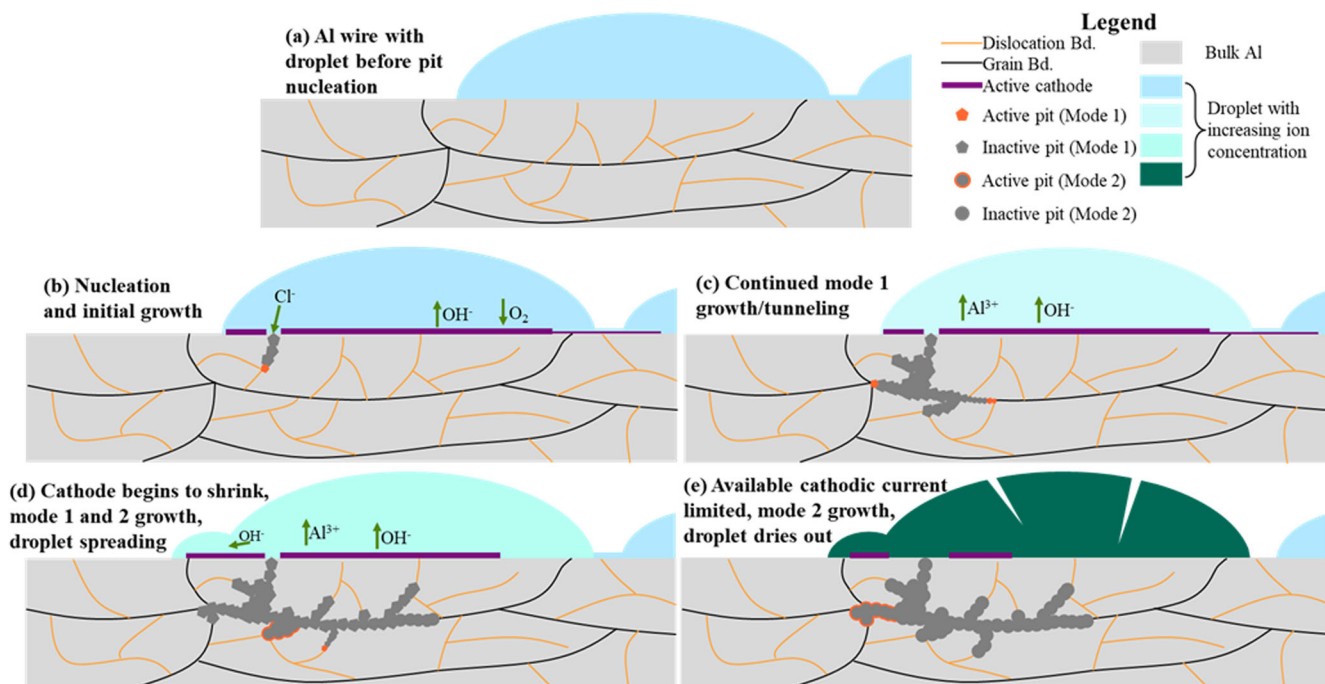


Fig. 9 A schematic of pit growth. A schematic outlining the likely lifecycle of pits in 4N Al under droplets of NaCl solution at 84% RH is provided in (a) to (e).

significant decrease in inter-droplet spacing, potentially facilitating droplet interconnection. Additionally, by affecting cathode efficiency, the susceptibility of the local microstructure to pitting may have played a role in the rate of pit growth⁵⁶. Thus, both microstructural features and droplet interconnectivity, in addition to droplet size, may affect pit growth rates.

The growth durations of six pits were greater than 19 h. The other five repassivated within, on average, 12 h after nucleation. No relationship between pit growth duration and either initial droplet size or initial pit growth rate was observed, see Fig. 5. Droplet spreading was associated with increased duration of pit growth, likely by increasing the size and/or efficiency of the cathode, see Fig. 5b.

Pit morphology also appeared to influence the duration of the secondary growth regime. Two pits were associated with prolonged secondary growth regimes compared to all others, 19 or more hours compared to ≈ 5 h. These two pits are highlighted in Fig. 5b. Both pits consisted of relatively few, elongated tendrils, e.g. compare Fig. 4 to Fig. 3. Relatively fewer, elongated tendrils would suggest a longer path for the diffusion of pit stabilizing species, causing a more confined and longer diffusion pathway, and keeping the Al passive film unstable for longer. As pit morphology appears to be a strong function of the underlying microstructure, we speculate that factors such as grain morphology may play a role in the duration of pit growth.

In all but one case, the rate of pit growth increased significantly after droplet spreading relative to the initial pit growth rate. A similar result was observed in commercial-purity Al and was attributed to an increase in cathode size created by droplet spreading¹⁹. Additionally, secondary droplets can act as more efficient cathodes than the initial droplet because of OH^- ions from the cathodic reaction allowing for elevated solution conductivity and oxygen solubility^{19,57,58}. To examine the potential for enhanced cathodic kinetics, the pH, solution conductivity, O_2 solubility, and solution density were calculated using OLI Studio (Ver. 10.0, MSE Database) for three cases: the initial droplet, which was assumed to contain only NaCl, the secondary droplet, which was assumed to contain only AlCl_3 , and a mixture of these

two. These calculations, provided in Supplementary Table 2, suggest an increase to solution conductivity and O_2 solubility in the secondary and mixed droplets which could increase the rate of corrosion and increase the transport limited current density, respectively⁵⁹.

When all individual pit volume growth is summed to show cumulative volume loss (directly proportional to mass loss) in Fig. 2b, the 4N-Al material had similar trends to other materials under atmospheric corrosion scenarios and constant contaminant environments where the corrosion rate slows over time^{41,60–62}. However, in the current study, the early stages of corrosion damage did not show the commonly described power law volume/mass loss relationship with time. Figure 2b instead shows a multi-step sigmoidal-like behavior. At the onset of the experiment, numerous pits nucleated (initial ramp in rate) and grew (linear region), followed by a brief plateau in growth (stifling of those pits). Subsequently, new pits nucleated, increasing the growth rate again. Intriguingly, the continuum level kinetics of volume-loss were remarkably similar to the growth kinetics of the fastest-growing individual pits, suggesting that the continuum-level rates of volume-loss were dominated by the growth rates of these pits. We note that inflection points in the cumulative data are smoothed over in typical corrosion mass or volume loss data due to their limited temporal resolution. Additionally, the present study characterized only 11 pits, while typical studies of mass or volume loss during atmospheric corrosion likely include many more pits and significantly larger surface areas than the 12.8 mm^2 inspected in this study. These results thus suggest that, with sufficiently fine temporal resolution, over a relatively small area, growth kinetics of individual pits could be approximated from continuum-level mass loss data. This could be useful in cases when damage caused by localized corrosion, e.g. pitting, is of concern.

Data from in-situ XCT allowed current density and pit stability products to be calculated for two pits, see Fig. 6. The “instantaneous” current densities were as large as 86 A/cm^2 , though were generally $\approx 5 \text{ A/cm}^2$, common values for active pitting regions⁶³. These are one to two orders of magnitude

greater than those measured by Glanvill et al. in AA2024²⁶ but are consistent with the current densities observed in Frankel's 2D pit measurements on thin film Al samples⁶⁴.

The measured (i.x) either meet or exceeded the range of (i.x) determined by others to be required for metastable and stable pits for Al^{30,31}. The measured (i.x) values in Fig. 6 ranging above and below the stable (i.x) value determined by Pride et al. complements the sporadic, largely unstable nature of the pits measured with XCT here. This study shows the temporal and spatial resolution of the XCT measurements here can accurately portray the electrochemical parameters specific to individual pits under corrosive atmospheric environments.

METHODS

Material

To study atmospheric corrosion kinetics in Al, a 0.813 mm diameter Al wire material was acquired from ESPI metals. The composition of this material (in ppm), measured using coupled plasma mass spectroscopy, was Mg 14, V < 1, Cu 23, Zn 16, Ti 5, Ga 2, Fe 42, Si 21, with the remainder being Al. We define the principal axes of this material as the fiber direction (FD), which is parallel to the length of the wire, and the radial direction (RAD), which is parallel to the wire diameter.

Two samples were extracted from this material to characterize the microstructure using scanning electron microscopy (SEM). One was sectioned perpendicular to the FD, the other parallel to the FD. The methods used to characterize these samples are presented in the following section. Secondary electron images were acquired from both samples and are provided in the Supplementary Material. Energy-dispersive X-ray spectroscopy (EDS) maps from both samples are presented in the Supplementary Material. Small ($\approx 1 \mu\text{m}$), widely spaced ($> 20 \mu\text{m}$) second-phase particles rich in Fe were observed in this material.

Electron backscatter diffraction (EBSD) data revealed that grains were elongated along the wire drawing direction (the FD) and contained residual dislocation structure. EBSD data from both specimens are presented as inverse pole figure (IPF) and kernel average misorientation (KAM) maps are provided in the Supplementary Material. KAM measures the misorientation between each point and all neighboring points within the kernel and is a commonly used way to visualize local misorientations in the microstructure created by grain boundaries and geometrically necessary dislocations⁶⁵. No cleanup methods were applied to EBSD data to remove unindexed pixels.

Microscopy

The microstructure of the Al material before corrosion was characterized using a Zeiss Supra 55VP field emission scanning electron microscope (SEM). All images, EDS data, and EBSD data were collected using an accelerating voltage of 20 kV. No phases other than Al were identified using EDS. Electron backscatter diffraction (EBSD) data was collected using Oxford HKL AZtecTM software. A stepsize of $0.5 \mu\text{m}$ was used. EBSD data were subsequently processed using MTEX⁶⁶, an extension for MATLAB. Adjacent points misoriented by less than 5° were assigned to the same grain. A minimum grain size of 10 points was enforced.

For 3D serial sectioning of a pit, a different microscope and data collection method was employed than was described in the prior paragraph. A pit from a sample was serial sectioned in a dual beam plasma focused ion beam (FIB)-SEM to characterize the microstructural features associated with this pit. This pit was identified and located using XCT data. Note that the methods for collecting XCT data and analyzing it are described in the subsequent section. The pit was serial-sectioned using a Helios 5 Laser PFIB. Each slice was 500 nm thick and EBSD data were collected using a 500 nm stepsize. EBSD data were collected using

Oxford HKL AZtecTM. An accelerating voltage of 5 kV was used. EBSD data were subsequently reconstructed and analyzed using DREAM3D⁶⁷ and visualized using Dragonfly and FIJI. Kernel average misorientation (KAM) maps were created from these EBSD data using a $2 \times 2 \times 2$ kernel size⁶⁵.

Specimen preparation

Four specimens of 4N-Al wire were prepared for in-situ characterization following the procedure described by Noell et al.¹⁹. Briefly, 25 mm specimens were cut from the as-received material and cleaned for 1.5 min in a 1.0 M NaOH at 60°C . They were then rinsed in deionized water, placed in 70% HNO_3 for 0.5 min, rinsed with deionized water, and dried using compressed air. Subsequently, a uniform field of discrete, picoliter-sized droplets each loaded with $200 \mu\text{g}/\text{cm}^2$ of NaCl was created across the entire surface of the wire using the inkjet printing method described in reference⁶⁸. Following salt printing, each wire was encapsulated in a plastic tube that contained a sponge, as described by Noell et al.¹⁹. For each specimen, immediately before beginning in-situ XCT characterization, a few droplets of super-saturated KCl were added to the sponge. This created an 84% RH atmosphere within the tube⁶⁹. This tube was subsequently sealed with epoxy, and the entire assembly was immediately placed within the XCT system for characterization. The top of the wire, i.e. the portion closest to the sponge, was identified. A 1.25 mm tall region 3 mm below this area was subsequently characterized using XCT for the remainder of the study, see next section for more details on XCT characterization. The temperature within the XCT system remained at room temperature, $25^\circ\text{C} \pm 3^\circ\text{C}$, throughout characterization. Following XCT characterization, samples were stored in a sealed jar that was maintained at 84% RH and remained at room temperature ($\approx 25^\circ\text{C}$) throughout the study. Samples were subsequently inspected periodically up to a year after this initial exposure. Note that all four samples were prepared and treated identically throughout the study.

In-situ XCT characterization and 3D XCT data analysis

XCT was performed using the Zeiss Xradia Versa 520 (Carl Zeiss XRM, Pleasanton, CA), a lab-based XCT system. All scans on all specimens were performed using the same settings: an accelerating voltage of 60 kV, a power of 5 W, no beam filter, and the 4X objective. The source to sample and sample to detector distances were changed to ensure an effective voxel size for all scans of $1.25 \mu\text{m}$. This gives an effective spatial resolution of $15.6 \mu\text{m}^3$ ($2 \times 2 \times 2$ voxels) for features in three dimensions.

For each sample, a 1.25 mm tall portion centered on a region 3 mm from the top of the wire was characterized. The total surface area of the sample characterized was thus 3.2 mm^2 . Within each sample, the same region was characterized throughout the experiment. For all samples, each scan of this section took approximately 80 min (1.33 h). The temporal resolution of in-situ datasets was thus 1.33 ± 0.67 h. To emphasize that measurements are not instantaneous, all results are reported with error bars showing ± 0.67 h.

To characterize this 1.25 mm tall portion of the sample, the sample was rotated 360° and a total of 1601 projections was taken. The exposure time for each projection was 2 s to ensure a minimum of 5000 counts through the thickest part of the wire, as recommended by Zeiss. Reference images, consisting of ten frames without a sample, were automatically collected during each tomography scan. This allowed radiographs within each scan to be normalized by subtracting this background. After each tomography scan completed, it was automatically reconstructed by the Zeiss XMReconstructor software using a standard filtered back-projection algorithm and collection of the next tomography dataset began.

All samples were characterized for the first 100 h after the sponge was saturated. Before the first tomography dataset was collected, a 1 h “warm-up” scan was performed to ensure that the X-ray source fully stabilized at the accelerating voltage. During subsequent data analysis, it was determined that no pits nucleated during this initial warm-up scan.

Reconstructed tomography datasets were processed and analyzed using the Dragonfly 3D Software 2021.1 (Object Research Systems Inc, Montreal, Canada, 2021). Phases of interest, such as pits and droplets, were segmented manually based on grayscale values and location. These measurements were used to evaluate pit volume and pit surface area.

DATA AVAILABILITY

The raw/processed data required to reproduce these findings cannot be shared at this time as the data also forms part of an ongoing study.

CODE AVAILABILITY

Codes are available upon request to the corresponding author(s).

Received: 27 September 2022; Accepted: 25 January 2023;
Published online: 16 February 2023

REFERENCES

- McCafferty, E. *Introduction To Corrosion Science* (Springer Science & Business Media, 2010).
- Örnek, C. et al. Time-dependent in situ measurement of atmospheric corrosion rates of duplex stainless steel wires. *NPJ Mater. Degrad.* **2**, 1–15 (2018).
- King, A., Johnson, G., Engelberg, D., Ludwig, W. & Marrow, J. Observations of intergranular stress corrosion cracking in a grain-mapped polycrystal. *Science* **321**, 382–385 (2008).
- Almuaili, F., McDonald, S., Withers, P. & Engelberg, D. Application of a quasi in situ experimental approach to estimate 3-D pitting corrosion kinetics in stainless steel. *J. Electrochem. Soc.* **163**, C745 (2016).
- Örnek, C. & Engelberg, D. Toward understanding the effects of strain and chloride deposition density on atmospheric chloride-induced stress corrosion cracking of type 304 austenitic stainless steel under MgCl₂ and FeCl₃: MgCl₂ droplets. *Corrosion* **75**, 167–182 (2019).
- Eguchi, K., Burnett, T. L. & Engelberg, D. L. X-ray tomographic observation of environmental assisted cracking in heat-treated lean duplex stainless steel. *Corros. Sci.* **184**, 109363 (2021).
- Eguchi, K., Burnett, T. L. & Engelberg, D. L. X-Ray tomographic characterisation of pitting corrosion in lean duplex stainless steel. *Corros. Sci.* **165**, 108406 (2020).
- Turnbull, A. Corrosion pitting and environmentally assisted small crack growth. *Proc. Math. Phys. Eng. Sci.* **470**, 20140254 (2014).
- Singh, S. et al. In situ investigation of high humidity stress corrosion cracking of 7075 aluminum alloy by three-dimensional (3D) X-ray synchrotron tomography. *Mater. Res. Lett.* **2**, 217–220 (2014).
- Singh, S. S., Stannard, T. J., Xiao, X. & Chawla, N. In situ X-ray microtomography of stress corrosion cracking and corrosion fatigue in aluminum alloys. *JOM* **69**, 1404–1414 (2017).
- Stannard, T. J. et al. 3D time-resolved observations of corrosion and corrosion-fatigue crack initiation and growth in peak-aged Al 7075 using synchrotron X-ray tomography. *Corros. Sci.* **138**, 340–352 (2018).
- Vallabhaneni, R., Stannard, T. J., Kaira, C. S. & Chawla, N. 3D X-ray microtomography and mechanical characterization of corrosion-induced damage in 7075 aluminium (Al) alloys. *Corros. Sci.* **139**, 97–113 (2018).
- Singh, S. S. et al. Measurement of localized corrosion rates at inclusion particles in AA7075 by in situ three dimensional (3D) X-ray synchrotron tomography. *Corros. Sci.* **104**, 330–335 (2016).
- Ramandi, H. L., Chen, H., Crosky, A. & Saydam, S. Interactions of stress corrosion cracks in cold drawn pearlitic steel wires: An X-ray micro-computed tomography study. *Corros. Sci.* **145**, 170–179 (2018).
- Bradley, R. et al. Time-lapse lab-based x-ray nano-CT study of corrosion damage. *J. Microsc.* **267**, 98–106 (2017).
- Almuaili, F., McDonald, S., Withers, P., Cook, A. & Engelberg, D. Strain-induced reactivation of corrosion pits in austenitic stainless steel. *Corros. Sci.* **125**, 12–19 (2017).
- Mohammed-Ali, H. B., Street, S. R., Attallah, M. M. & Davenport, A. J. Effect of microstructure on the morphology of atmospheric corrosion pits in type 304L stainless steel. *Corrosion* **74**, 1373–1384 (2018).
- Alwitt, R., Uchi, H., Beck, T. & Alkire, R. Electrochemical tunnel etching of aluminum. *J. Electrochem. Soc.* **131**, 13 (1984).
- Noell, P. J., Schindelholz, E. J. & Melia, M. A. Revealing the growth kinetics of atmospheric corrosion pitting in aluminum via in situ microtomography. *NPJ Mater. Degrad.* **4**, 1–10 (2020).
- Weirich, T. D. et al. Humidity effects on pitting of ground stainless steel exposed to sea salt particles. *J. Electrochem. Soc.* **166**, C3477–C3487 (2019).
- Niverty, S., Kale, C., Solanki, K. N. & Chawla, N. Multiscale investigation of corrosion damage initiation and propagation in AA7075-T651 alloy using correlative microscopy. *Corros. Sci.* **185**, 109429 (2021).
- Knight, S., Salazar, M. & Trueman, A. The study of intergranular corrosion in aircraft aluminium alloys using X-ray tomography. *Corros. Sci.* **53**, 727–734 (2011).
- Eckermann, F. et al. In situ monitoring of corrosion processes within the bulk of AlMgSi alloys using X-ray microtomography. *Corros. Sci.* **50**, 3455–3466 (2008).
- Knight, S. et al. In situ X-ray tomography of intergranular corrosion of 2024 and 7050 aluminium alloys. *Corros. Sci.* **52**, 3855–3860 (2010).
- Davenport, A. et al. Mechanistic studies of atmospheric pitting corrosion of stainless steel for ILW containers. *Corros. Eng. Sci. Technol.* **49**, 514–520 (2014).
- Glanvill, S. J., du Plessis, A., Street, S. R., Rayment, T. & Davenport, A. J. In situ X-ray tomography observations of initiation and propagation of pits during atmospheric corrosion of aluminium alloy AA2024. *J. Electrochem. Soc.* **168**, 031508 (2021).
- Hansen, N. & Mehl, R. F. New discoveries in deformed metals. *Metall. Mater. Trans. A* **32**, 2917–2935 (2001).
- Bentea, L., Watzky, M. A. & Finke, R. G. Sigmoidal nucleation and growth curves across nature fit by the Finke–Watzky model of slow continuous nucleation and autocatalytic growth: explicit formulas for the lag and growth times plus other key insights. *J. Phys. Chem. C* **121**, 5302–5312 (2017).
- Myhrvold, N. P. Revisiting the estimation of dinosaur growth rates. *PLoS ONE* **8**, e81917 (2013).
- Pride, S., Scully, J. & Hudson, J. Metastable pitting of aluminum and criteria for the transition to stable pit growth. *J. Electrochem. Soc.* **141**, 3028 (1994).
- Sridhar, G., Birbilis, N. & Raja, V. The reliability of metastable pit sizes estimated from dissolution current in aluminium alloys. *Corros. Sci.* **182**, 109276 (2021).
- McCafferty, E. Sequence of steps in the pitting of aluminum by chloride ions. *Corros. Sci.* **45**, 1421–1438 (2003).
- Zavadil, K. R., Ohlhausen, J. & Kotula, P. Nanoscale void nucleation and growth in the passive oxide on aluminum as a pre-pitting process. *J. Electrochem. Soc.* **153**, B296 (2006).
- Street, S. R., Cook, A. J., Mohammed-Ali, H. B., Rayment, T. & Davenport, A. J. The Effect of Deposition Conditions on Atmospheric Pitting Corrosion Location Under Evans Droplets on Type 304L Stainless Steel. *Corrosion* **74**, 520–529 (2018).
- Morton, S. & Frankel, G. Atmospheric pitting corrosion of AA7075-T6 under evaporating droplets with and without inhibitors. *Mater. Corros.* **65**, 351–361 (2014).
- Thomson, M. & Frankel, G. Atmospheric pitting corrosion studies of AA7075-T6 under electrolyte droplets: part I. Effects of droplet size, concentration, composition, and sample aging. *J. Electrochem. Soc.* **164**, C653 (2017).
- Li, J., Maier, B. & Frankel, G. Corrosion of an Al–Mg–Si alloy under MgCl₂ solution droplets. *Corros. Sci.* **53**, 2142–2151 (2011).
- Yasuda, M., Weinberg, F. & Tromans, D. Pitting corrosion of Al and Al–Cu single crystals. *J. Electrochem. Soc.* **137**, 3708 (1990).
- Maier, B. & Frankel, G. Pitting corrosion of bare stainless steel 304 under chloride solution droplets. *J. Electrochem. Soc.* **157**, C302 (2010).
- Chen, Z. & Kelly, R. Computational modeling of bounding conditions for pit size on stainless steel in atmospheric environments. *J. Electrochem. Soc.* **157**, C69 (2009).
- Schaller, R. F., Jove-Colon, C. F., Taylor, J. M. & Schindelholz, E. J. The controlling role of sodium and carbonate on the atmospheric corrosion rate of aluminum. *NPJ Mater. Degrad.* **1**, 1–8 (2017).
- Murer, N. & Buchheit, R. Stochastic modeling of pitting corrosion in aluminum alloys. *Corros. Sci.* **69**, 139–148 (2013).
- Newman, R. Local chemistry considerations in the tunnelling corrosion of aluminium. *Corros. Sci.* **37**, 527–533 (1995).
- Baumgärtner, M. & Kaesche, H. Aluminum pitting in chloride solutions: morphology and pit growth kinetics. *Corros. Sci.* **31**, 231–236 (1990).
- Lee, D. N. & Seo, J. H. Orientation dependent directed etching of aluminum. *Corros. Sci. Technol.* **8**, 93–102 (2009).
- Pearson, E., Huff, H. & Hay, R. A metallographic study of pitting corrosion induced in 28 aluminum by exposure to tap water. *Can. J. Technol.* **30**, 311 (1952).
- Katona, R. et al. Quantitative assessment of environmental phenomena on maximum pit size predictions in marine environments. *Electrochim. Acta* **370**, 137696 (2021).

48. Galvele, J. R. Transport processes and the mechanism of pitting of metals. *J. Electrochem. Soc.* **123**, 464 (1976).
49. Liang, H., Liu, J., Schaller, R. F. & Asselin, E. A new corrosion mechanism for X100 pipeline steel under oil-covered chloride droplets. *Corrosion* **74**, 947–957 (2018).
50. Tsuru, T., Tamiya, K.-I. & Nishikata, A. Formation and growth of micro-droplets during the initial stage of atmospheric corrosion. *Electrochim. Acta* **49**, 2709–2715 (2004).
51. Zhang, J., Wang, J. & Wang, Y. Micro-droplets formation during the deliquescence of salt particles in atmosphere. *Corrosion* **61**, 1167–1172 (2005).
52. Gray, J. The kinetics of growth. *J. Exp. Biol.* **6**, 248–274 (1929).
53. Melchers, R. E. A review of trends for corrosion loss and pit depth in longer-term exposures. *Corros. Mater. Degrad.* **1**, 42–58 (2018).
54. Mouloudi, M., Radouani, R., Essahli, M., Chafi, M. & Chhiba, M. Study of corrosion pit propagation in aluminum by numerical simulation using the finite element method. *Int J. Electrochem. Sci.* **16**, 21–119 (2021).
55. Liu, C. & Kelly, R. G. A review of the application of finite element method (FEM) to localized corrosion modeling. *Corrosion* **75**, 1285–1299 (2019).
56. Birbilis, N. & Buchheit, R. G. Electrochemical characteristics of intermetallic phases in aluminum alloys: an experimental survey and discussion. *J. Electrochem. Soc.* **152**, B140 (2005).
57. Tang, X., Ma, C. R., Orazem, M. E., You, C. & Li, Y. Local electrochemical characteristics of pure iron under a saline droplet II: Local corrosion kinetics. *Electrochim. Acta* **354**, 136631 (2020).
58. Tsutsumi, Y., Nishikata, A. & Tsuru, T. Pitting corrosion mechanism of Type 304 stainless steel under a droplet of chloride solutions. *Corros. Sci.* **49**, 1394–1407 (2007).
59. Cui, F., Presuel-Moreno, F. J. & Kelly, R. G. Computational modeling of cathodic limitations on localized corrosion of wetted SS 316L at room temperature. *Corros. Sci.* **47**, 2987–3005 (2005).
60. Blücher, D. B., Lindström, R., Svensson, J. & Johansson, L. The effect of CO₂ on the NaCl-induced atmospheric corrosion of aluminum. *J. Electrochem. Soc.* **148**, B127–B131 (2001).
61. Melchers, R. Pitting corrosion of mild steel in marine immersion environment part 1: maximum pit depth. *Corrosion* **60**, 824–836 (2004).
62. Srinivasan, J. et al. Long-term effects of humidity on stainless steel pitting in sea salt exposures. *J. Electrochem. Soc.* **168**, 021501 (2021).
63. Laycock, N. & White, S. Computer simulation of single pit propagation in stainless steel under potentiostatic control. *J. Electrochem. Soc.* **148**, B264 (2001).
64. Frankel, G. The growth of 2-D pits in thin film aluminum. *Corros. Sci.* **30**, 1203–1218 (1990).
65. Wright, S. I., Nowell, M. M. & Field, D. P. A review of strain analysis using electron backscatter diffraction. *Microsc. Microanal.* **17**, 316–329 (2011).
66. Bachmann, F., Hielscher, R. & Schaeben, H. Texture analysis with MTEX—free and open source software toolbox. In *Solid state phenomena* (Vol. 160, pp. 63–68). (Trans Tech Publications Ltd., 2010).
67. Groeber, M. A. & Jackson, M. A. DREAM. 3D: a digital representation environment for the analysis of microstructure in 3D. *Integr. Mater. Manuf. Innov.* **3**, 56–72 (2014).
68. Schindelholz, E. & Kelly, R. Application of inkjet printing for depositing salt prior to atmospheric corrosion testing. *Electrochem. Solid-State Lett.* **13**, C29 (2010).
69. Greenspan, L. Humidity fixed points of binary saturated aqueous solutions. *J. Res. Natl Bur. Stand. Sec. A* **81**, 89–96 (1977).

ACKNOWLEDGEMENTS

The authors would like to acknowledge James Griego, Priya Pathare, and Jason Taylor. Supported by the Laboratory Directed Research and Development program at Sandia National Laboratories, a multimission laboratory managed and operated by National Technology and Engineering Solutions of Sandia LLC, a wholly owned subsidiary of Honeywell International Inc. for the U.S. Department of Energy's National Nuclear Security Administration under contract DE-NA0003525. The views expressed in the article do not necessarily represent the views of the U.S. DOE or the United States Government.

AUTHOR CONTRIBUTIONS

P.J.N., I.C., R.M.K., and M.A.M. performed in-situ XCT experiments and analysis of XCT data. E.K. and M.A.M. performed microscopy of corroded samples. P.J.N., M.A.M., A.T.P., and E.J.S. performed analysis of microscopy data. All authors discussed and contributed to the writing of the paper.

COMPETING INTERESTS

The authors declare no competing interests.

ADDITIONAL INFORMATION

Supplementary information The online version contains supplementary material available at <https://doi.org/10.1038/s41529-023-00328-7>.

Correspondence and requests for materials should be addressed to Philip J. Noell.

Reprints and permission information is available at <http://www.nature.com/reprints>

Publisher's note Springer Nature remains neutral with regard to jurisdictional claims in published maps and institutional affiliations.



Open Access This article is licensed under a Creative Commons Attribution 4.0 International License, which permits use, sharing, adaptation, distribution and reproduction in any medium or format, as long as you give appropriate credit to the original author(s) and the source, provide a link to the Creative Commons license, and indicate if changes were made. The images or other third party material in this article are included in the article's Creative Commons license, unless indicated otherwise in a credit line to the material. If material is not included in the article's Creative Commons license and your intended use is not permitted by statutory regulation or exceeds the permitted use, you will need to obtain permission directly from the copyright holder. To view a copy of this license, visit <http://creativecommons.org/licenses/by/4.0/>.

© The Author(s) 2023